

Phase Transitions of $S = 1$ Spinor Condensates in an Optical Lattice

Daniel Podolsky^{1,2}, Shailesh Chandrasekharan³ and Ashvin Vishwanath^{2,4}

¹*Department of Physics, Technion, 32000 Haifa, Israel*

²*Department of Physics, University of California, Berkeley, CA 94720*

³*Department of Physics, Box 90305, Duke University, Durham, NC 27708*

⁴*Materials Sciences Division, Lawrence Berkeley National Laboratory, Berkeley, CA 94720*

(Dated: Printed November 4, 2009)

We study the phase diagram of spin-one polar condensates in a two dimensional optical lattice with magnetic anisotropy. We show that the topological binding of vorticity to nematic disclinations allows for a rich variety of phase transitions. These include Kosterlitz-Thouless-like transitions with a superfluid stiffness jump that can be experimentally tuned to take a *continuous* set of values, and a new *cascaded Kosterlitz-Thouless* transition, characterized by *two* divergent length scales. For higher integer spin bosons S , the thermal phase transition out of the planar polar phase is strongly affected by the parity of S .

I. INTRODUCTION

Low temperature superfluidity in simple atomic systems is a well-studied subject. It is well-known that scalar bosons, confined to two spatial dimensions ($2d$), cannot form a true condensate. Instead, the off-diagonal correlations display either power law decay (in the superfluid phase) or exponential decay (in the normal phase). These two phases are usually separated by a finite temperature Kosterlitz-Thouless (KT) driven by superfluid vortex unbinding. Such a transition in atomic systems has been observed experimentally through interference measurements.¹

Atomic systems of bosons with degenerate hyperfine levels lead to more exotic phenomena at low temperatures usually referred to as “spinor condensation”. Such systems have been at the focus of intense experimental and theoretical activity since their discovery.² The hyperfine levels give rise to a new quantum number analogous to the spin. The macroscopic phase coherence in spinor systems can be accompanied by magnetic order. Indeed the spin and charge degrees of freedom may be strongly intertwined – as seen, for example, in the topological defects, which can simultaneously involve atomic supercurrents and magnetic textures.³ The presence of these multiple types of defects leads to a richer variety of phases and phase transitions.

In this paper, we study thermal transitions in $2d$ polar condensates, where uniaxial spin nematic order (characterized by a headless vector, or “director”) coexists with superfluidity. First, we point out a crucial difference between polar condensates with even integer and odd integer spin (as in $S = 1$ ^{23}Na). For even S , the superfluid vortex and the nematic disclination are independent, while for odd S they are bound to each other topologically. This strongly impacts the phase diagrams. When the nematic director is confined to rotate in a plane, the normal state can be reached via a single continuous transition from the polar state for the case of odd S , but not for even S , where a split transition is expected. We study the odd S case in detail in this paper, and further show that the single continuous transition it-

self can take on two very different characters, one, which is essentially KT-like, but with a non-universal superfluid stiffness jump; and another that is of a new ‘cascaded-KT’ type described in more detail below. Interference experiments¹ which have been used to study KT transitions in scalar condensates, can also be used to probe the new transitions discussed here.

Consider spin-one bosons in a $2d$ optical lattice, described by a Hubbard model with couplings U_0 and U_2 ,

$$\mathcal{H} = -t \sum_{\langle ij \rangle, \sigma} a_{i\sigma}^\dagger a_{j\sigma} + U_0 \sum_i n_i(n_i - 1) - \mu \sum_i n_i + U_2 \sum_i (\vec{S}_i^2 - 2n_i) - g \sum_i (S_i^z)^2. \quad (1)$$

The depth of the optical lattice serves to tune (U_0/t) . Here $a_{i\sigma}^\dagger$ creates an atom at site i with spin $S_i^z = \sigma \in \{-1, 0, 1\}$, n_i is the particle number at site i , and μ is the chemical potential. The quadratic Zeeman field g , described below, is absent in magnetically isotropic systems. We concentrate on atoms with antiferromagnetic spin interactions, $U_2 > 0$, *e.g.* as is the case in ^{23}Na .

The zero temperature phase diagram of model (1) with $U_2 > 0$ and $g = 0$ was studied in Ref. [4]. At unit filling (one atom per lattice site), the system undergoes a continuous transition at $T = 0$ between a nematic Mott insulator and a polar superfluid. The transition is tuned by the depth of the optical lattice. For deep lattices ($U_0/t \gg 1$) the system is a nematic Mott insulator, characterized by atoms which predominantly occupy the $S_z = 0$ state, together with a vanishing compressibility. More generally, the nematic can be any $\hat{n} \cdot \vec{S} = 0$ state, with the director \hat{n} serving as an order parameter. On the other hand, for weak optical lattices ($U_0/t \ll 1$) the system is a polar superfluid. The order parameter $\Psi_\sigma \equiv \langle a_\sigma \rangle = (\psi_{+1}, \psi_0, \psi_{-1})^T$ in the polar state is $\Psi = e^{i\theta} \mathcal{R}(0, 1, 0)^T - \mathcal{R}$ is a generic $SO(3)$ spin rotation. As in the Mott insulator, the polar state Ψ has nematic order, described by a director \hat{n} for which $\hat{n} \cdot \vec{S}|\Psi\rangle = 0$, but it *also* has superfluid order, captured by an expectation value of the superfluid phase θ .

In the following, we are interested in systems with pos-

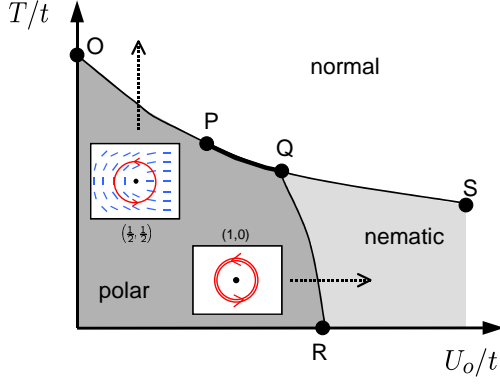


FIG. 1: Schematic phase diagram as a function of optical lattice depth and temperature. The topological defects that disorder the polar state are: a superfluid vortex $(q_c, q_s) = (1, 0)$, where θ winds by 2π (red double circle); and a disclination+half-vortex $(\frac{1}{2}, \frac{1}{2})$, where both θ and ϕ wind by π . Along the cascaded KT transition PQ , both defects play a role.

itive quadratic Zeeman field $g > 0$. Such a field has the effect of restricting the director \hat{n} to lie in the xy -plane in both the Mott nematic and polar states.² The most general planar polar state is then

$$\Psi = e^{i\theta} (-e^{i\phi}, 0, e^{-i\phi})^T, \quad (2)$$

where ϕ is the angle of \hat{n} relative to the x -axis. The AC Zeeman effect – shining linearly polarized light at a frequency slightly detuned from the hyperfine level splitting – can induce the required negative quadratic Zeeman field⁵ that leads to a planar polar state. The opposite $g < 0$ limit, (induced by a magnetic field in $S=1$ ^{23}Na) is essentially identical to a non-magnetic system since the nematic director is frozen along the field.

II. TOPOLOGICAL DEFECTS

Topological defects play an essential role in $2d$ finite temperature continuous phase transitions. In the present context, the planar polar SF is the “most ordered” phase, as it has both nematic and superfluid quasi long range order (QLRO). We can then understand the phase diagram in terms of proliferation of defects of the planar polar condensate, which can destroy the order partially (leading to a nematic insulator) or completely.

It is impossible to distinguish between the states $\pm\hat{n}$ (\hat{n} is a headless vector). However, an adiabatic rotation taking \hat{n} to $-\hat{n}$ induces a change of sign in the polar order parameter Ψ . This sign can be absorbed by simultaneously shifting the superfluid phase θ by π . Therefore, to insure single-valuedness of the order parameter, in a polar state, a nematic disclination must be accompanied by a half-vortex in the superfluid phase.

More generally, the topological point defects of a planar polar condensate in $2d$ are labeled by two half-

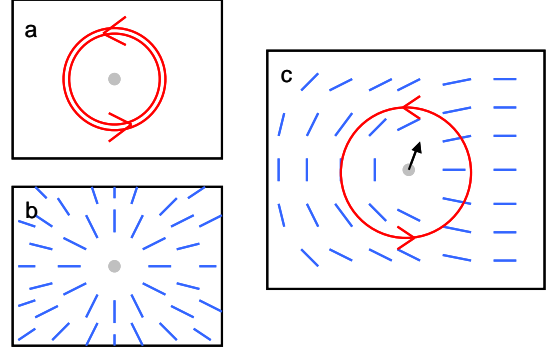


FIG. 2: Topological defects of the planar polar state. (a) In a superfluid vortex $(q_c, q_s) = (1, 0)$, θ_c winds by 2π around the vortex (superflow shown as double circle with arrows). (b) In a nematic vortex $(0, 1)$, the director \hat{n} winds by 2π . (c) In a disclination+half-vortex $(\frac{1}{2}, \frac{1}{2})$, \hat{n} and θ_c wind by π simultaneously.

integer charges, (q_c, q_s) , describing the winding of θ and ϕ , respectively, in units of 2π . By single-valuedness of Ψ in Eq. (2), the sum $q_c + q_s$ is constrained to be an integer. The lowest energy defects are the superfluid vortex $(\pm 1, 0)$, the nematic vortex $(0, \pm 1)$, and the disclination+half-vortex $(\pm \frac{1}{2}, \pm \frac{1}{2})$. These defects are shown in Fig. 2.

Topological defects proliferate when the temperature is large relative to some appropriate stiffness parameter. In the case at hand, due to the presence of both spin and charge degrees of freedom, there are two relevant stiffness coefficients, K_s and K_c . These correspond to the energy cost of an elastic deformation in the nematic direction ϕ and in the superfluid phase θ , respectively. In a dilute gas and in the absence of an optical lattice, the kinetic term $\frac{\hbar^2}{2m} |\nabla \Psi|^2 = \frac{\hbar^2}{2m} |\Psi|^2 \{(\nabla \theta)^2 + (\nabla \phi)^2\}$ predicts $K_c = K_s$.⁶ On the other hand, enhanced quantum fluctuations in an optical lattice can change this.⁷ An optical lattice suppresses both K_c and K_s , but its main effect is to impede atomic motion, leading to $K_c/K_s < 1$. For strong lattice potentials at integer filling, *i.e.* in the Mott nematic phase, the charge stiffness is suppressed to the point where the system is an insulator, while maintaining nematic QLRO.⁴ The nematic Mott insulator-polar SF transition is second order. Thus, proximity to this transition allows tuning the ratio $K_c/K_s \leq 1$ over a wide range.

The topological defects interact logarithmically at long distances, leading to a Coulomb gas action,

$$S = \sum_{ij} (K_c q_i^c q_j^c + K_s q_i^s q_j^s) \log \frac{r_{ij}}{a} + \sum_i \log y_i \quad (3)$$

Here, a is the defect core size, and the reduced stiffnesses $K_c = \frac{\pi \rho_c}{2T}$ and $K_s = \frac{\pi \rho_s}{2T}$ have been normalized by a factor of $2/\pi$ for later convenience. The defect fugacity y_i takes the values y_c and y_m , respectively, for the defects $(\pm 1, 0)$ and $(\pm \frac{1}{2}, \pm \frac{1}{2})$ in Fig. 2.

III. DEFECT UNBINDING

The phase diagram as a function of the reduced stiffnesses K_s and K_c consists of four phases: (i) *Polar state*.– At large K_s and K_c , all defects remain bound and the polar order parameter has algebraic order. (ii) *Disordered*.– In the opposite limit, when both K_s and K_c are small, all of the topological defects proliferate, and the system has short-range correlations in both charge and spin. (iii) *Nematic*.– Starting in the polar state and keeping K_s large, when K_c is reduced sufficiently, superfluid vortices proliferate, with all other defects remaining bound. This leads to algebraic order in the nematic order parameter $e^{2i\phi}$, but no superfluidity. (iv) *Paired superfluid*.– Conversely, when K_c is large and K_s is small, the nematic vortex unbinds, leading to algebraic order in $e^{2i\theta}$, but no spin order. Note that, for polar condensates in an optical lattice, for which $K_s > K_c$, the paired superfluid is not present, as shown in Fig. 1.

The phase boundaries of the polar state can be obtained from the requirement that all defects in Fig. 2 be bound. This corresponds to $K_c^R > 1$ (bound superfluid vortices), $K_s^R > 1$ (bound nematic vortices), and $K_c^R + K_s^R > 4$ (bound disclination+half-vortices). Here we have introduced the notation $K_{c,s}^R$ to denote the long-distance spin and charge stiffness, which is renormalized by the presence of a finite density of bound defect pairs. The conditions for vortex unbinding are shown in Fig. 3.

To obtain the correct phase diagram, however, it is important to recognize that *the conditions for defect unbinding cannot always be treated independently of one another*. In particular, there are situations where the unbinding of one type of defect can precipitate the unbinding of a second type of defect. As an example, consider the triangular region enclosed by **PQS** in Fig. 3. At first glance, it looks like the superfluid vortices are proliferated (since $K_c < 1$) whereas the disclination+half-vortices remain bound (since $K_c + K_s > 4$). This would identify this region as belonging to the nematic phase. However, points within this region cannot describe a stable nematic phase. The cheapest defects inside a nematic are the single disclinations – in which the phase ϕ winds by π . Disclinations are bound whenever the reduced spin stiffness K_s is larger than 4. However, $K_s < 4$ in the region **PQS**. Therefore, this region is part of the disordered phase.

The instability of the nematic within region **PQS** can also be understood by thinking of the single disclination as the remnant of the disclination+half-vortex of the polar phase, once the superfluid phase has been disordered due to the proliferation of superfluid vortices. In this situation, the proliferation of superfluid vortices renormalizes the charge stiffness to zero ($K_c^R = 0$). Therefore, although the bare values of K_c and K_s satisfy the condition for disclination+half-vortex to be bound, $K_c + K_s > 4$, the renormalized stiffnesses do not, $K_c^R + K_s^R < 4$. These arguments show that, along the line **PQ** (and also along **P'Q'**), the system undergoes a direct transition from the

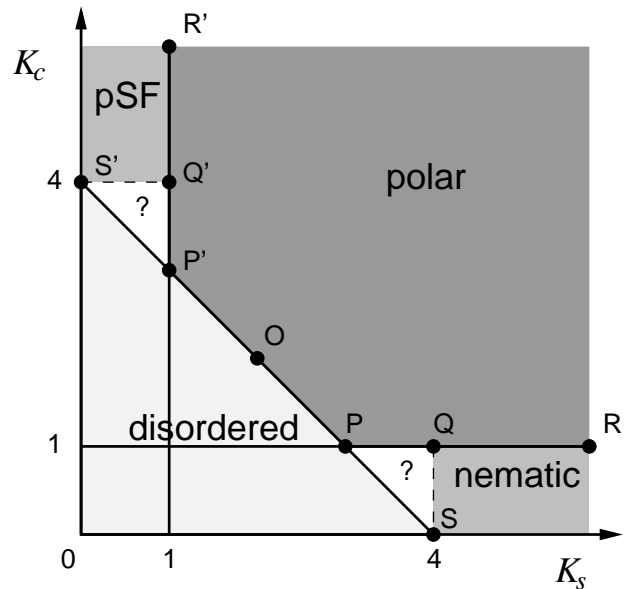


FIG. 3: Phase diagram as a function of the reduced stiffnesses K_c and K_s . The solid lines represent the conditions for the different topological defects to be bound, when the interactions between different types of defects are ignored. Two regions (enclosed by **PQS** and **P'Q'S'**) are labeled by question marks. In the absence of vortex interactions, these regions would be in the nematic and paired superfluid phases (pSF), respectively. However, as argued in the text, the ordered phases in these two regions are unstable, and the two regions are part of the disordered phase, which extends to the dashed lines **QS** and **Q'S'**. For simplicity, the phase diagram is drawn for infinitesimal bare defect fugacities. Point **O** is not a special point in the phase diagram, but it is indicated for comparison with Fig. 1

polar state to the disordered state. This transition involves two different types of defects, and therefore is in a different universality class from the transition along **P'OP**. We call the transition along **PQ** a “cascaded Kosterlitz-Thouless” transition (cKT).

It is difficult to give a fully controlled renormalization group (RG) treatment of the cKT transition, since the physics involves the proliferation of one type of defect before the other defect “realizes” that it is unbound. The conventional RG treatment of defect unbinding is only controlled when the defect fugacities are small, and it breaks down when the defects proliferate and the fugacities become large. Note that, despite the difficulty in giving a carefully controlled RG treatment, the coarse graining process in the RG cannot *increase* the value of the stiffnesses. Therefore the argument for the instability of nematic order within the region **PQS** is robust. In the following section, we will study the RG equations and derive the critical properties of the cKT transition **PQ**, and we will contrast it to the disclination+half-vortex proliferation along **P'OP**. This will be followed in Sec. V by a numerical study of the transitions along **PQ** and **P'OP** using Monte Carlo simulations. This will allow us to

study the finite size scaling properties at the two transitions, and compare them with the predictions from the RG analysis.

IV. RENORMALIZATION GROUP ANALYSIS

A. Renormalization group equations

In this section we focus on the case $K_s \geq K_c$, corresponding to bosons in an optical lattice. Then, the nematic vortices $(0, 1)$ are always the last defects to proliferate, and they can be neglected in the analysis below. A real space renormalization group (RG) analysis of the Coulomb gas (3) is carried out in Ref. [8]. To quadratic order in the fugacities,⁸

$$\dot{y}_c = 2(1 - K_c)y_c + 2\pi y_m^2 \quad (4a)$$

$$\dot{y}_m = (4 - K_s - K_c)y_m/2 + 2\pi y_m y_c \quad (4b)$$

$$\dot{K}_c = -8\pi K_c^2(2y_c^2 + y_m^2) \quad (4c)$$

$$\dot{K}_s = -8\pi K_s^2 y_m^2 \quad (4d)$$

Here $\dot{g} = \frac{dg}{d\ell}$ and e^ℓ is the length rescaling factor. These RG equations are valid provided the fugacities remain small. As is clear from Eq. (3), the RG equations must be symmetric under the exchange of spin and charge degrees of freedom.

In order to understand the RG equations (4), consider first the flow of the superfluid vortex fugacity y_c , Eq. (4a). The first term on the RHS describes the competition between energy cost and entropy gain for the creation of a superfluid vortex; the second term, proportional to y_m^2 , arises because two dislocation+half-vortices can combine into a superfluid vortex. On the other hand, Eq. (4c) for the flow of K_c describes the screening of the Coulomb interaction between defects due to a finite density of bound defect-anti-defect pairs in the medium. The sign of the flow of K_c is negative semi-definite, and is only zero when the fugacities y_c and y_m are zero, or when K_c itself is zero. Thus, the fixed point in the RG requires either the fugacities or K_c to flow to zero. Similar considerations apply to K_s . The fixed points of the RG are characterized by the values of the renormalized stiffness $K_\gamma^R \equiv K_\gamma(\ell = \infty)$, ($\gamma = c, s$).

The continuous transitions between the phases in Fig. 1 arise from defect unbinding, and may be classified according to the type of defect that triggers the transition. If a single type of defect is important, one observes a conventional KT scenario. However, we also find a class of transitions where unbinding of one set of defects triggers the instability in another set, leading to a cascaded KT transition with two diverging length scales. Here, we will concentrate on the two direct transitions between the polar and disordered states, along the lines **OP** and **PQ**. The multicritical point **P** belongs to a different universality class, as discussed in Ref. [8]. The other transitions **QR** and **QS** belong in the conventional KT scenario.

B. Disclination+half-vortex unbinding (OP)

Here, the polar state is disordered by the proliferation of disclination+half-vortices. These defects destroy both charge and spin order. At the transition, the renormalized stiffness satisfy $K_s^R + K_c^R = 4$ and $K_c^R > 1$. The superfluid stiffness jump in this transition can be tuned *continuously* with optical lattice depth, ranging from $K_c^R = 2$ at point **O**, to $K_c^R \rightarrow 1$ as we approach point **P**. On the other hand, the sum of superfluid and spin stiffness is universal. The correlation lengths ξ_γ diverge as the transition is approached from the disordered side as

$$\xi_\gamma \sim a \exp \left[d_\gamma (T - T_{KT})^{-\frac{1}{2}} \right]. \quad (5)$$

As in the usual KT transition, $d_c = d_s$ is non-universal.

C. Cascaded KT criticality (PQ)

Along **PQ**, the superfluid vortices are on the verge of proliferating, since $K_c^R = 1$. On the other hand, the sum $K_s^R + K_c^R$ is above the threshold value of 4, indicating that the disclination+half-vortices are bound at the transition. However, as soon as the transition is crossed, K_c flows to zero, reducing $K_s^R + K_c^R$ below 4. Now, the disclination+half-vortices unbind, leading to a completely disordered phase. We call this a “cascaded” KT (cKT) transition, since unbinding of one type of defect triggers the unbinding of the other.

Both spin-nematic and charge orders have diverging correlation lengths as **PQ** is approached from the disordered phase. However, there is a separation of scales $\xi_s \gg \xi_c$, due to the fact that the superfluid vortices unbind at a shorter length scale than the disclination+half-vortices. We will show below that the two are related by a power law,

$$\xi_s \sim a(\xi_c/a)^B, \quad (6)$$

where $B = 1/(4 - K_s^R) > 1$, and ξ_c follows Eq. (5).

The main challenge in studying the cascaded KT transition is that the naive RG equations (4) break down once the superfluid vortices unbind. In order to circumvent this, we use the separation of scales to perform the RG in two steps. First, we solve Eq. (4) up to the scale ξ_c where the superfluid vortex fugacity begins to diverge. At this point, the superfluid correlations are explicitly short-ranged, and we can integrate out the charge degrees of freedom to obtain a local spin-only model. We then study the RG flow of the ensuing spin model.

In the first step, the fugacity of the disclination+half-vortex is renormalized down according to Eq. (4b), $\tilde{y}_m \sim y_m(a/\xi_c)^{(K_s-3)/2}$. The RG flow of the coarse grained couplings \tilde{y}_m , and \tilde{K}_c at longer scales is then governed by $\dot{\tilde{y}}_m = \frac{1}{2}(4 - \tilde{K}_s)\tilde{y}_m$ and $\dot{\tilde{K}}_s = -8\pi\tilde{K}_s^2\tilde{y}_m^2$. Integrating this RG flow until \tilde{y}_m is of order unity yields Eq. (6),

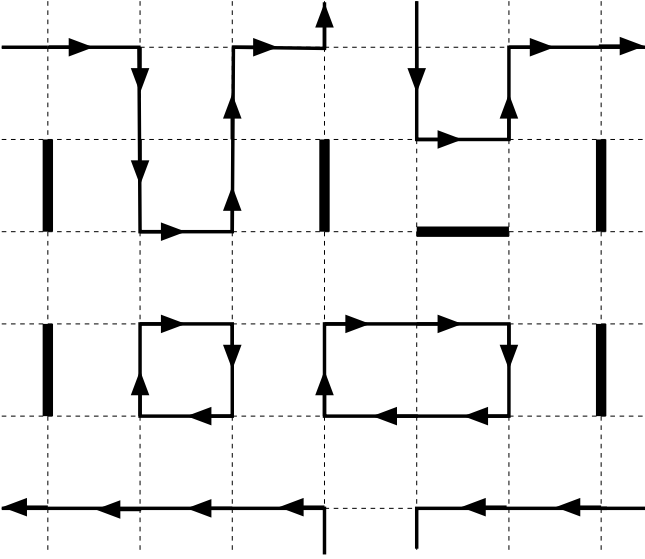


FIG. 4: An illustration of a current loop configuration discussed in the text. The bonds with arrows are the directed dimers and solid undirected bonds are the undirected double dimers. The configuration shown is planar, while in the model studied here the configurations will be similar but on a cubical lattice.

with $B = (4 - K_s^R)^{-1}$. Note that B is bounded below by one, near point **P**, and can be arbitrarily large near **Q**, where $K_s^R = 4$. The topology of the phase diagram in Fig. 1 is crucially different from Ref. [8], where the cKT transition (**PQ**) is misinterpreted as two separate transitions.

The *two* diverging length scales at the cKT transition arise due to the fact that the disclination+half-vortex is a dangerously irrelevant operator at the transition. This is one of the few examples we know of a dangerously irrelevant *disorder* operator.^{9,10}

V. MONTE CARLO SIMULATIONS

A. Loop model

In order to test the new transitions predicted in the previous sections, we introduce a relatively simple lattice current-loop model defined on a periodic cubic lattice. The configurations $[\mathcal{C}]$ that contribute to its partition function contain two types of bond variables: directed dimers $e_{i,\alpha} \in \{1, 0, -1\}$ and undirected double dimers $d_{i,\alpha} \in \{0, 2\}$, on bonds between site i and its neighbors $i + \hat{\alpha}$ ($\alpha = x, y, \tau$). At each site i we enforce two constraints: (1) $\sum_{\alpha} \{e_{i,\alpha} + e_{i-\hat{\alpha},\alpha}\} = 0$ (directed dimer conservation) and (2) $\sum_{\alpha} \{|e_{i,\alpha}| + d_{i,\alpha} + |e_{i-\hat{\alpha},\alpha}| + d_{i-\hat{\alpha},\alpha}\} = 2$ (close packing constraint). The partition function is given by

$$Z = \sum_{\mathcal{C}} \prod_i \{W_D\}^{(d_{i,x}+d_{i,y}+d_{i,\tau})/2} \{t\}^{|e_{i,\tau}|+d_{i,\tau}}. \quad (7)$$

Roughly, the parameter t is a temperature-like parameter (raising t eliminates in-plane loops and double dimers), while W_D tunes the ratio K_c/K_s (increasing W_D increases the double dimer density). As an illustration we show a planar lattice configuration in figure 4. Configurations that contribute to the partition function are similar configurations but on a cubic lattice of size $L \times L \times 4$.

The loop model (7) is a simple variant of strongly coupled two color lattice QCD with staggered fermions (SCLQCD2), a model with an $SO(3) \times U(1)$ symmetry and hence of interest also in the field of spinor condensates. In the model we consider here, the $SO(3)$ symmetry is broken to an $SO(2)$ subgroup. While SCLQCD2 has been studied in both cubic (3d)¹¹ and hyper-cubic (4d)¹² lattices, the above model remains unstudied so far. These models can be studied efficiently using directed-loop Monte Carlo algorithms as discussed in Refs.12 and 13.

As a consequence of the constraints, the model considered here has two conserved currents: (1) $J_{i,\alpha}^s = \eta_i \{|e_{i,\alpha}| + d_{i,\alpha} - 1/3\}$ where $\eta_i = +1$ and -1 on alternating sites, and (2) $J_{i,\alpha}^c = e_{i,\alpha}$. These currents correspond to the spin and charge conservation and can be used to compute K_s and K_c :

$$K_\gamma = \frac{\pi}{2L^2} \left\langle \left(\sum_i J_{i,x}^a \right)^2 \right\rangle. \quad (8)$$

Here, K_γ is normalized such that at a usual KT transition one would expect $K_s, K_c = 1$. Note that at every space-like link, $J_{i,\alpha}^c + J_{i,\alpha}^s$ is an *even* integer¹⁹. This implies that the topological defects are half-integers with the constraint that $q_c + q_s$ is an integer, which is crucial to the physics here²⁰. In Appendix A we provide a diquark representation of the loop model, in which the symmetries of the model are seen explicitly. Due to these symmetries, the model studied here is expected to exhibit the same universal physics as the Coulomb gas system described by Eq. (3) close to second order phase transitions. In fact we will provide below clear numerical evidence for the predicted transitions along the line **OP** (disclination+half vortex unbinding) and **PQ** (cKT transition) using this model.

B. Disclination+half-vortex proliferation (**P'OP**)

Let us first focus on the transition that occurs along the line **P'OP**. When one is exactly on this line, the finite size scaling formula for K_a , can be computed using RG and is given by

$$K_a(T_{KT}, L) = K_a^R \left(1 + \frac{1}{2} \frac{1}{C_a + \log L} \right), \quad (9)$$

where $K_c^R + K_s^R = 4$ and the C_a ($a = c, s$) are non-universal constants. We would like to show evidence for this using our model. We have discovered that in our

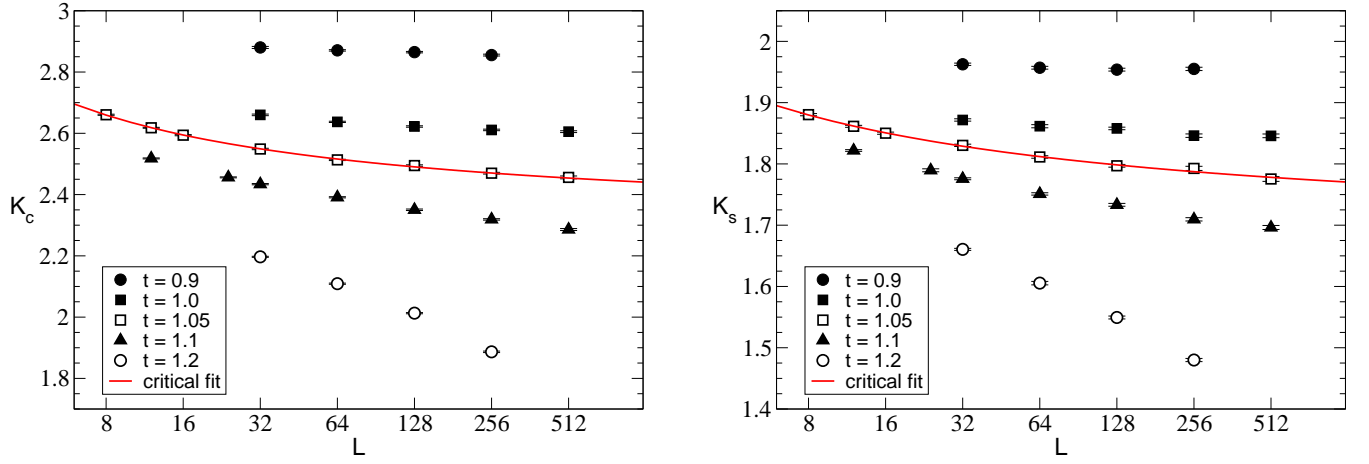


FIG. 5: Finite size scaling near the polar melting transition (**P'O P**) at $W_D = 0$ and $t = 0.9, 1.0, 1.05, 1.1$ and 1.2 . The solid line is the fit to Eq. (9). The values of the fit are given in table I

model we can approach this line by varying t for fixed W_D in the interval $0 \leq W_D < 3$. We have done extensive calculations up to lattice sizes of $L = 512$ by focusing on $W_D = 0$ and 1 . In Fig. 5 we show the finite size scaling of K_s and K_c at $W_D = 0$ for various values of t close to the transition. Table I shows that we obtain a good fit to Eq. (9) for $t \leq 1.05$. This is understandable since everywhere inside the polar phase K_a is expected to be a constant for large L and this just means C_a is large. Since $t = 1.05$ is the last value of t where the fit works well, at that value we should be very close to the critical line. It is important to note that indeed $K_c + K_s \approx 4$ there (see last column of table I). Individually each of the K_a 's are not universal. Since $K_c^R > K_s^R$ we must be

somewhere on the **P'O** line of the phase diagram. We can change W_D and t to go to a different point on the **P'O P** line. To show this we have performed calculations at $W_D = 1$. In table I we also give some of our fits for the $W_D = 1$ case. Again $t = 1.05$ seems to be on the critical line and $K_c + K_s \approx 4$. But now we have $K_c = K_s$ which means we are right at the midpoint **O**.

C. Cascaded KT transition (PQ)

Next we focus on the cascaded KT transition line **PQ**. On this line the cKT scenario predicts that K_s and K_c should follow different finite size scaling laws:

$$K_c(t_{cKT}, L) = 1 + \frac{1}{2} \frac{1}{C_c + \log L}, \quad (10)$$

$$K_s(t_{cKT}, L) = K_s^R + C_s L^{3-K_s^R}, \quad (11)$$

where C_γ are again non-universal constants, and $3 < K_s^R < 4$. In order to test this scenario, the first step is to locate a point on the cKT line within our model. We have identified numerically that one such point is $W_D = 3.05$ and $t = t_{cKT} \equiv 0.885$. In order to cross the transition line at this point we vary both W_D and t such that $W_D = 3.05 + 10(t - 0.885)$, and compute K_s and K_c for lattice sizes up to $L = 512$.

Figure 6 shows our data for both K_c and K_s . The first important qualitative observation we make from the figure is that both K_s and K_c appear to jump to zero for $t > t_{cKT}$ as expected. Further the rough value of the jump is $K_c^R \approx 1$ and $K_s^R \approx 3.6$ which is again as expected. Thus, the point is roughly midway between **P** and **Q**, yet in the numerical data, both K_s and K_c seem to undergo a transition *simultaneously*. This is consistent with the results of Sec. III, where we argued that for these

t	K_c^R	C_c	χ^2	K_s^R	C_s	χ^2	$K_s^R + K_c^R$
$W_D = 0$							
0.80	2.96(2)	7(1)	0.3	1.95(2)	∞	0.7	4.9(4)
0.90	2.74(1)	6.5(9)	0.3	1.89(1)	10(2)	0.9	4.63(2)
1.00	2.468(5)	3.1(2)	1.6	1.763(5)	4.7(5)	1.1	4.231(10)
1.05	2.297(2)	1.09(3)	0.9	1.677(2)	2.05(7)	0.7	3.974(4)
1.10	2.145(2)	0.34(2)	24.7	1.594(2)	0.98(4)	4.4	3.739(4)
$W_D = 1$							
0.80	2.651(1)	∞	1.4	2.652(1)	∞	1.3	5.316(3)
0.90	2.41(2)	15(5)	0.6	2.40(1)	12(3)	1.1	4.81(3)
1.00	2.138(6)	4.2(4)	1.3	2.144(9)	4.6(7)	2.3	4.282(15)
1.05	1.967(2)	1.29(3)	2.6	1.968(2)	1.29(5)	2.3	3.935(4)
1.10	1.821(1)	0.43(2)	59	1.818(2)	0.40(2)	24	3.639(3)

TABLE I: Fits to Eq. (9) at $W_D = 0$ and $W_D = 1$. Note that $t = 1.05$ is almost on the **P'O P** line, with $K_s^R + K_c^R \approx 4$ with goodness of fit $\chi^2/DOF \approx 1-2$. When $W_D = 1$ and $t = 1.05$ we are at the midpoint **O** on the **P'O P** line.

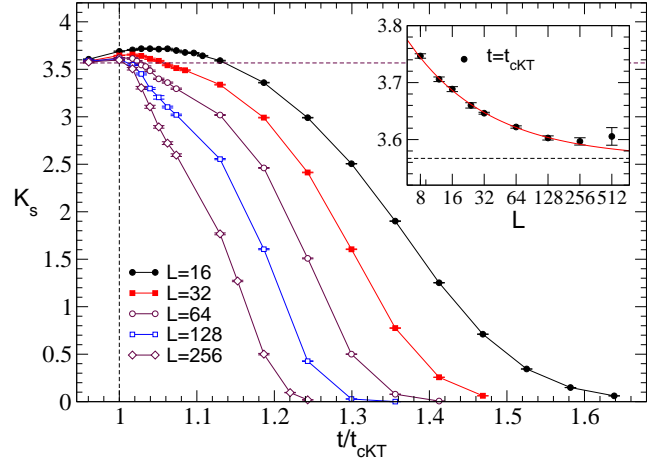
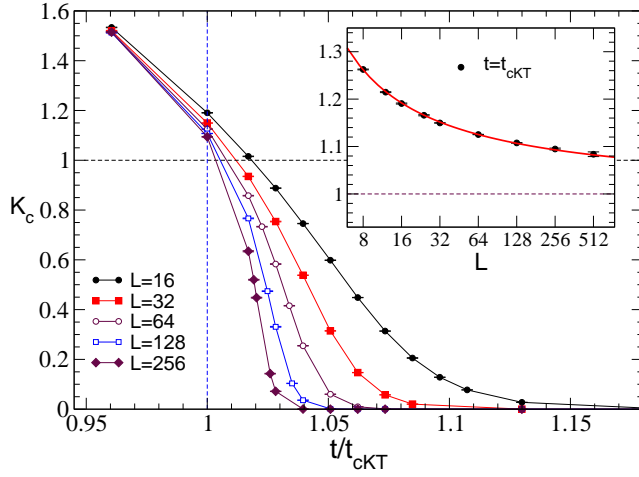


FIG. 6: Cascaded KT (**PQ**): K_c (top) and K_s (bottom) vs. t/t_{cKT} for various system sizes L . **Insets:** K_c and K_s vs. L at fixed $t = t_{cKT}$, fit to Eqs. (10) and (11), respectively. The fits yield $K_s^R = 3.567(3)$, $C_s = 0.58(2)$, and $C_c = -0.168(4)$, with goodness of fit $\chi^2/DOF \sim 1$.

parameters a split transition *i.e.* crossing **QR** first and then **QS** is ruled out since $K_s^R < 4$ is inconsistent with a stable nematic phase.

Next we perform a more quantitative analysis at $t = t_{cKT}$. We fit our data for K_c and K_s as a function of L to Eqs. (10) and (11). If $K_c^R = 1$ is fixed we find $C_c = -0.168(4)$, with goodness of fit $\chi^2/DOF = 1$, and $K_s^R = 3.567(3)$, and $C_s = 0.58(2)$ with $\chi^2/DOF = 0.7$. We emphasize that $8 \leq L \leq 512$ were used in the fit. This large range gives us confidence in our analysis. The insets in the graphs in Fig. 6 show the finite size scaling of K_c and K_s , respectively along with the fit. Thus, we claim that the Monte Carlo simulations are consistent with the expected finite size scaling predicted by the RG analysis.

Another important prediction of the cKT scenario is the presence of two diverging correlation lengths near the cKT transition **PQ**, which follows Eq. (6). Unfortunately we have not measured the correlation lengths directly. However we can see this divergence in an indirect manner. Since a finite size box limits the diverging correlation lengths, the jumps in the stiffness K_a are no longer sharp but broadened depending on the value of L (see Fig. 6). A temperature $t_a^* > t_{KT}$ can then be defined such that $K_a(t_a^*) = xK_a^R(t_{KT})$ where $x < 1$ is some fixed fraction. In other words, at t_a^* , K_a has been reduced to a fraction x of its value at t_{KT} . The fact that the correlation length diverges as t approaches t_{KT} is now seen by the fact that as L becomes large t_a^* approaches t_{KT} . This behavior can be quantified using RG and we expect

$$\frac{1}{\sqrt{t_a^* - t_{KT}}} = \alpha_a \log L + \beta_a \quad (12)$$

where all constants are non-universal, except for the ratio $\alpha_c/\alpha_s = 1/(4 - K_s^R)$. Note that Eq. (12) is valid provided

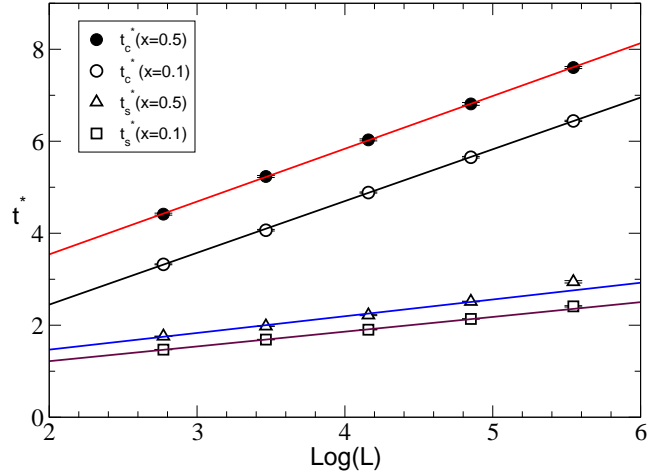


FIG. 7: $(t_a^* - t_{KT})^{-1/2}$ vs. system size for charge correlations and spin correlations at $x = 0.1$ and $x = 0.5$. The solid lines are fits given in table II

that $t_a^* - t_{KT}$ is small, *i.e.* for large enough system size L .

Fig. 7 shows our data for t_a^* for the choices $x = 0.1$ and $x = 0.5$. The first striking qualitative observation we make is that $1/\sqrt{t_a^* - t_{KT}}$ scales linearly with $\log(L)$ to a very good approximation as expected. Further the slopes of the two lines are clearly different. Note that we expect $\xi_s \sim \xi_c^p$ where $p = \alpha_c/\alpha_s > 1$. Indeed we do find that $p > 1$. Quantitatively, while t_c^* fits well to Eq. (12), t_s^* does not fit for larger values of L due to a small but clear curvature in the data. Table II contains the fit results. Ignoring the large values of χ^2/DOF , we see that $\alpha_c/\alpha_s \sim 3.5$ at $x = 0.1$ and ~ 3.2 at $x = 0.5$. These must be compared to the theoretical prediction

x	α_s	β_s	χ^2/DOF	α_c	β_c	χ^2/DOF
0.1	0.321(2)	0.577(8)	8.3	1.125(5)	0.20(2)	1.4
0.5	0.363(3)	0.74(1)	35	1.15(1)	1.25(4)	0.3

TABLE II: Fits to Eq. (12) at $x = 0.1$ and $x = 0.5$. The fits for t_s^* are not very good because of a detectable curvature in the data.

from the RG treatment, $1/(4 - K_s^R) = 2.31(1)$. If we take the curvature in t_s^* into account by using a fit of the form $\frac{1}{\sqrt{t_s^* - t_{KT}}} = \alpha_s \log L + \beta_s + \gamma_s/(\log L)$ the χ^2/DOF improves slightly but is still not good. The ratio α_c/α_s changes to about 3 and 2.3 at $x = 0.1$ and 0.5. If instead we just use the last two points and draw a straight line through the data, this ratio is 2.8 and 1.85 respectively. This large variation in the values of the ratio α_c/α_s shows that we do not yet have quantitative control on it. The theoretical expectation seems to be within the large systematic errors. Since our data are obtained on rather small lattice sizes where the two large length scales $\xi_s \sim \xi_c^{2.3}$ cannot fit well, our inability to quantitatively control the ratio is not surprising.

VI. CONCLUSION

In conclusion, we have shown that the topological binding of spin and charge vorticity in $S = 1$ polar condensates can give new types of phase transitions. In particular we have shown the existence of the disclination+half vortex unbinding transition, which is similar to the KT transition but where the superfluid stiffness jump is non-universal and a cascaded KT transition where in addition to a non-universal jump in the stiffness two correlation lengths diverge at the critical point, where one is a power of the other. A large scale numerical study supports the detailed picture we have developed.

Our analysis can be applied to other ordered states. For example, spin-2 ^{87}Rb in a magnetic field forms a “square nematic” state^{15,16} with $\Psi \sim e^{i\theta}(e^{2i\phi_s}, 0, 0, 0, e^{-2i\phi_s})$. This yields precisely the same physics as the spin-1 planar polar state. There are examples outside of cold atomic systems which display the same topological structure studied here. For instance, Berg *et al.* have argued that the thermal melting of a striped superconducting state is produced by a fully analogous set of topological defects to those discussed here.¹⁷ Therefore, the phase diagram of a striped superconductor is the same as that of a planar polar condensate, although the particular phases involved in the two cases are different. Following this work, a recent numerical study has looked at the 3d version of this system.¹⁸

We thank E. Berg, G. Delfino, J.E. Moore, S. Mukerjee, L. Radzihovsky, and D. Stamper-Kurn for useful discussions. This work was supported in part by the NSF grant DMR-0506953 and the Hellman Faculty Fund.

APPENDIX A: DIQUARK REPRESENTATION OF THE LOOP MODEL

In this Appendix, we recast the loop model Eq. (7) in terms of a path integral over Grassmann variables in order to clarify the symmetries of the model. The partition function is given by

$$Z_G = \int \mathcal{D}\psi_\uparrow \mathcal{D}\psi_\downarrow \mathcal{D}\bar{\psi}_\downarrow \mathcal{D}\bar{\psi}_\uparrow e^{-S_G} \quad (\text{A1})$$

where the action

$$S_G = - \sum_{i,\alpha} \left[\frac{u_\alpha}{2} \left\{ (\bar{\Psi}_{i+\alpha} \Psi_i)^2 + (\bar{\Psi}_i \Psi_{i+\hat{\alpha}})^2 \right\} + (W_D - 1) \left(\frac{u_\alpha}{2} \right)^2 (\bar{\Psi}_{i+\alpha} \Psi_i)^2 (\bar{\Psi}_i \Psi_{i+\hat{\alpha}})^2 \right].$$

Here

$$\Psi_i \equiv \begin{pmatrix} \psi_{i,\uparrow} \\ \psi_{i,\downarrow} \end{pmatrix}, \quad \text{and} \quad \bar{\Psi}_i \equiv \begin{pmatrix} \bar{\psi}_{i,\uparrow} & \bar{\psi}_{i,\downarrow} \end{pmatrix} \quad (\text{A2})$$

such that $\psi_{i\sigma}$ and $\bar{\psi}_{i\sigma}$ ($\sigma = \uparrow, \downarrow$) are independent Grassmann variables residing on the sites of a $L \times L \times 4$ lattice. In particular, $\psi_{i\sigma}$ and $\bar{\psi}_{i\sigma}$ are *not* complex conjugates of each other. The constants u_α are $u_x = u_y = 1$ and $u_\tau = t$, so that $\hat{\tau}$ can be thought of as an Euclidean time direction and t as a temperature-like parameter. Performing the path integral over $\psi_{i\sigma}$ and $\bar{\psi}_{i\sigma}$ yields the loop model (7) exactly, as can be checked easily by explicit computation.

Equation (A1) can also be expressed as a model of “diquarks” $D_i \equiv \psi_{i\downarrow} \psi_{i\uparrow}$ and $\bar{D}_i \equiv \bar{\psi}_{i\uparrow} \bar{\psi}_{i\downarrow}$ hopping and interacting on a lattice,

$$S_G = \sum_{i,\alpha} u_\alpha (\bar{D}_i D_{i+\alpha} + \bar{D}_{i+\alpha} D_i) - (W_D - 1) \sum_{i,\alpha} u_\alpha^2 \bar{D}_i D_i \bar{D}_{i+\alpha} D_{i+\alpha}. \quad (\text{A3})$$

The model has an $\text{SU}(2) \times \text{SU}(2)$ gauge symmetry. To see this, note that the diquark $D_i = \psi_{i\downarrow} \psi_{i\uparrow} = \frac{1}{2} \epsilon_{\sigma\sigma'} \psi_{i\sigma} \psi_{i\sigma'}$ is invariant under a *local* transformation

$$\Psi_i \rightarrow U_i \Psi_i, \quad (\text{A4})$$

where $U_i \in \text{SU}(2)$. Similarly, an independent $\text{SU}(2)$ transformation \bar{U}_i can be carried out on the barred variables, $\bar{\Psi}_i \rightarrow \bar{\Psi}_i \bar{U}_i^\dagger$, leaving \bar{D}_i invariant.

After taking the gauge invariance into account, we are still left with an independent *global* $\text{U}(1) \times \text{U}(1)$ symmetry of the model (A1), parametrized by the angles θ and ϕ ,

$$\begin{aligned} \Psi_i &\rightarrow e^{i(\eta_i \phi - \theta)/2} \Psi_i \\ \bar{\Psi}_i &\rightarrow e^{i(\eta_i \phi + \theta)/2} \bar{\Psi}_i \end{aligned} \quad (\text{A5})$$

where $\eta_i = +1$ and -1 on alternating sites. Note that, unlike the gauge invariance in Eq. (A4), the transformation (A5) does not leave the diquark invariant, since $\psi_{i\downarrow}\psi_{i\uparrow} \rightarrow e^{i(\eta_i\phi-\theta)}\psi_{i\downarrow}\psi_{i\uparrow}$. However, a simultaneous shift of θ and ϕ by the angle π does leave the diquark invariant. Hence, the model (A1) is explicitly seen to have topological defects that are labeled by half-integers with

the constraint that $q_c + q_s$ is an integer. Therefore, the low energy defects of the model are the superfluid vortex $(1, 0)$, the nematic vortex $(0, 1)$, and the nematic+half-vortex $(\frac{1}{2}, \frac{1}{2})$. By equivalence of the diquark model to Eq. (7), we conclude that the loop model also has the same topological defects.

-
- ¹ Z. Hadzibabic *et al.*, Nature **441**, 1118 (2006).
² J. Stenger *et al.*, Nature **396**, 345 (1998).
³ T.L. Ho, Phys. Rev. Lett. **81**, 742 (1998); T. Ohmi and K. Machida, J. Phys. Soc. Jpn. **67**, 1822 (1998); F. Zhou, Phys. Rev. Lett. **87**, 080401 (2001).
⁴ A. Imambekov, M. Lukin, and E. Demler, Phys. Rev. A **68**, 063602 (2003).
⁵ D. Stamper-Kurn, private communication.
⁶ S. Mukerjee, C. Xu, and J.E. Moore, Phys. Rev. Lett. **97**, 120406 (2006).
⁷ M.D. Barret, J.A. Sauer, and M.S. Chapman, Phys. Rev. Lett. **87**, 010404 (2001).
⁸ F. Krüger and S. Scheidl, Phys. Rev. Lett. **89**, 095701 (2002).
⁹ S. Ostlund and B.I. Halperin, Phys. Rev. **B23**, 355 (1981).
¹⁰ T. Senthil, A. Vishwanath, L. Balents, S. Sachdev and M. P. A. Fisher Science **303**, 1490 (2004).
¹¹ S. Chandrasekharan, Phys. Rev. Lett. **97**, 182001 (2006).
¹² S. Chandrasekharan and F.-J. Jiang, Phys. Rev. **D74**, 14506 (2006);
¹³ D.H. Adams and S. Chandrasekharan, Nucl. Phys **B662**, 220 (2003).
¹⁴ M. Hasenbusch, A. Pelissetto, and E. Vicari, J.Stat.Mech. **0512**, 002 (2005).
¹⁵ H. Schmaljohann *et al.*, Phys. Rev. Lett. **92**, 040402 (2004).
¹⁶ A. Turner *et al.*, Phys. Rev. Lett. **98**, 190404 (2007).
¹⁷ E. Berg, S. Kivelson, and E. Fradkin, Nature Phys. **5**, 830 (2009).
¹⁸ E.K. Dahl *et al.*, Phys. Rev. B **77**, 144519 (2008).
¹⁹ Strictly speaking, $J_{i,\alpha}^c + J_{i,\alpha}^s$ is not an integer due to the staggered factor $\eta_i/3$. However, the topological defects are determined from the sum of $J_{i,\alpha}^c + J_{i,\alpha}^s$ over the four values of the time-like coordinate at fixed space coordinates. The staggered factor drops out from the sum, which is then an even integer.
²⁰ Models based on $U(1)\times U(1)$ continuous symmetry, but with different discrete symmetries than discussed here, have been shown to display different critical properties, as discussed *e.g.* in Ref.14